CrossMark

Helium Abundance of the Sun: A Spectroscopic Analysis

Satyajeet Moharana[1,2] , B. P. Hema[2] , and Gajendra Pandey[2]

[1] Indian Institute of Science Education and Research, Berhampur, 760003, India; satyajeetm19@iiserbpr.ac.in
[2] Indian Institute of Astrophysics; Bengaluru, 560034, India; hema.bp@iiap.res.in, pandey@iiap.res.in

Abstract

Determining the He/H ratio in cool stars presents a fundamental astrophysical challenge. While this ratio is established for hot O and B stars, its extrapolation to cool stars remains uncertain due to the absence of helium lines in their observed spectra. We address this knowledge gap by focusing on the Sun as a representative cool star. We conduct spectroscopic analyses of the observed solar photospheric lines by utilizing a combination of MgH molecular lines and neutral Mg atomic lines including yet another combination of CH and C_2 molecular lines with neutral C atomic lines. Our spectroscopic analyses were further exploited by adopting solar model atmospheres constructed for distinct He/H ratios to determine the solar photospheric helium abundance. The helium abundance is determined by enforcing the fact that for an adopted model atmosphere with an appropriate He/H ratio, the derived Mg abundance from the neutral Mg atomic lines and that from the MgH molecular lines must be the same. The same holds for the C abundance derived from neutral C atomic lines and that from CH lines of the CH molecular band and C_2 lines from the C_2 Swan band. The estimated He/H ratio for the Sun is discussed based on the one-dimensional local thermodynamic equilibrium model atmosphere. The helium abundance (He/H $= 0.091^{+0.019}_{-0.014}$) obtained for the Sun serves as a critical reference point to characterize the He/H ratio of cool stars across the range in their effective temperature.

1. Introduction

Fundamentally, elemental abundances of all astrophysical entities are compared against their solar values. This makes the chemical composition of the Sun a benchmark and an essential reference in the field of astronomy and astrophysics including cosmology, astroparticle, space, and geophysics. Over a century, advances have been made in characterizing the complete solar composition from the significant studies of Russell (1929), Suess & Urey (1956), Goldberg et al. (1960), Lambert (1968, 1978), Anders & Grevesse (1989), and Grevesse & Sauval (1998) to the more recent studies of Lodders (2003), Asplund et al. (2005a, 2009, 2021), and Caffau et al. (2011). In this context, it is worth noting Allende Prieto (2020) that gives an overview of the advances and the way forward in spectroscopic analysis.

However, spectroscopic determination of helium abundance, i.e., $\log \epsilon(\mathrm{He})$, or the helium-to-hydrogen (He/H) ratio, in the solar photosphere has always remained a fundamental astrophysical challenge due to the absence of helium line transitions in the photospheric absorption spectrum of the Sun. Though measurement of solar helium abundance can be obtained from observing coronal sources, including the solar cosmic rays (Lambert 1967), solar wind (Ogilvie & Wilkerson 1969), and solar energetic particles (Reames 2021) or from the chromospheric line intensities (Hirshberg 1973), these measurements do not essentially demonstrate the photospheric helium content; for example, one possible reason may be due to the first ionization potential effect as discussed in Laming (2015).

Anders & Grevesse (1989) derived the protosolar helium content ($\log \epsilon(\mathrm{He}) = 10.99$) from H II regions and B-type stars, which share similar metallicity as that of the Sun. This determination led to the adoption of a He/H ratio of 0.1 ($\log \epsilon(\mathrm{He}) = 11.00$) for model atmospheres used in solar abundance analysis over the years, under the assumption that this ratio remains consistent across both hot and cool stars. The adopted helium abundance is in good agreement with that of a recent study by Nieva & Przybilla (2012) for early B stars.

Solar helium abundance has been estimated from indirect methods; one is through helioseismology that determines the He/H ratio accurately in the solar convection zone by analyzing the second ionization region of helium (Basu & Antia 2004; Monteiro & Thompson 2005; Houdek & Gough 2007). This method, however, is sensitive toward the adopted equation of state (Basu & Antia 2008) and the assumed metallicity of the reference solar model. The important problem is that the predictions of the standard solar model, for the adopted downward revised solar abundances of Asplund et al. (2009), do not agree with the helioseismic determinations of the sound speed, the depth of the convection zone, and the abundance of helium in this layer.

In this study we have adopted a novel technique, similar to that described by Hema et al. (2020) for cool giants, to spectroscopically determine the solar photospheric He/H ratio. This new method was the outcome of our earlier two studies: Hema & Pandey (2014) and Hema et al. (2018). In the following sections, we describe the solar spectrum, the adopted model atmospheres, and the abundance analysis procedure.

2. The Solar Spectrum

For this study, we have used a high-resolution, high signal-to-noise ratio solar spectrum that is from the National Solar

Observatory archives. This solar flux spectrum, as documented by Kurucz et al. ([1984](#)), was observed using the McMath–Pierce solar telescope equipped with a Fourier transform spectrometer (FTS). The spectrum has a resolving power R ($\lambda/\Delta\lambda$) $\sim$ 400,000 and a signal-to-noise ratio of about 1000 per pixel in the wavelength range 3400–9300 Å. The observation involved directing unfocused sunlight from the solar heliostat into the FTS instrument. This method captures the solar disk in its entirety, effectively representing the Sun as a star in our observations (Hinkle et al. [2000](#)).

This FTS solar spectrum was used by Allende Prieto & Garcia Lopez ([1998](#)) to compile a precise wavelength catalog in the optical spectrum of the Sun. Additionally, the equivalent widths measured from this spectrum are in excellent agreement with other solar spectrum studies that have been referred to in this paper.

3. Abundance Analysis

The observed solar spectrum, as discussed above, is analyzed in local thermodynamic equilibrium (LTE) using a radiative transfer code MOOG (Sneden et al. [2012](#)) combined with a star's model atmosphere to compute the absorption spectrum or to predict the equivalent width of an absorption line. In this study we have adopted ATLAS12 model atmospheres with different He/H ratios. These model atmospheres were computed based on the plane-parallel and LTE approximation by taking into account the line-blanketing effect; see Kurucz ([2014](#)) and Hema et al. ([2020](#)) for details.

To adopt a model atmosphere computed for the normal He/H ratio of 0.1, the input abundances of H and He required by MOOG are $\log \epsilon(\mathrm{H}) = 12.00$ and $\log \epsilon(\mathrm{He}) = 11.00$. Similarly, for a model atmosphere computed for a He/H ratio of 0.125, the input abundances of H and He, which need to be provided to MOOG, are $\log \epsilon(\mathrm{H}) = 11.974$ and $\log \epsilon(\mathrm{He}) = 11.071$. These input abundances of H and He for different He/H ratios are calculated by utilizing a standard normalization relation (Equation ([1](#))):

$$\sum_i \mu_i E_i = \mu_{\mathrm{H}}\mathrm{H} + \mu_{\mathrm{He}}\mathrm{He} + \sum_{i=3} \mu_i E_i = 10^{12.15}, \quad (1)$$

where $\mu_i E_i$ represents the total mass of an element E, having atomic number i present in the stellar photosphere, with μ_i and E_i denoting the atomic mass and abundance by number for the element E, respectively. Assuming that H and He are the primary components of the stellar photosphere, while all other elements present are in trace amounts (Equation ([2](#))), i.e.,

$$\sum_{i=3} \mu_i E_i \rightarrow 0, \quad (2)$$

$\mathrm{H} + 4\mathrm{He} = 10^{12.15}$ since $\mu_{\mathrm{H}} = 1$ and $\mu_{\mathrm{He}} = 4$. Note that, conventionally, log of H is $\log \epsilon(\mathrm{H})$, and log of He is $\log \epsilon(\mathrm{He})$ or, in general, log of E is $\log \epsilon(\mathrm{E})$.

3.1. Adopted Solar Parameters

The solar parameters, such as effective temperature (T_{eff}), surface gravity ($\log g$), and metallicity ([Fe/H]) were adopted from Asplund et al. ([2021](#)) and Gray ([2021](#)), as $T_{\mathrm{eff}} = 5773 \pm 16$ K, $\log g = 4.4374 \pm 0.0005$ (cgs), and [Fe/H] = 0.0. We have also adopted a microturbulence (ξ_{t}) of 1 km s^{-1} as suggested by Asplund et al. ([2021](#)).
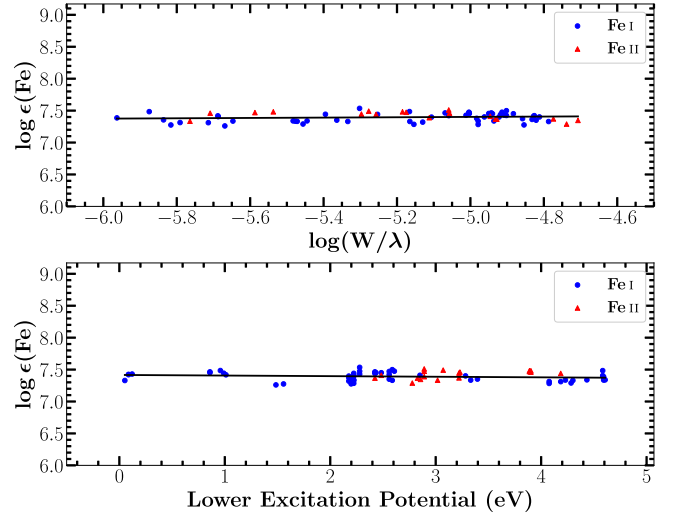

Figure 1. $\log \epsilon(\mathrm{Fe})$ vs. $\log(W/\lambda)$ for the adopted $\xi_{\mathrm{t}} = 1.0$ km s^{-1} (top panel). $\log \epsilon(\mathrm{Fe})$ vs. lower excitation potential (LEP) for the adopted (T_{eff}, $\log g$) = (5773 K, 4.44 cgs) (bottom panel).

3.2. Equivalent Width Analyses and Spectrum Syntheses

To validate the adopted solar parameters, an abundance analysis was performed on the observed solar photospheric spectrum. Neutral and singly ionized absorption lines of iron (Fe I and Fe II) were used as probes to verify the excitation and the ionization balance including the adopted microturbulence. The Fe I and Fe II lines are taken from Asplund et al. ([2000](#)). Abundances of iron were derived from the measured equivalent widths of Fe I and Fe II lines by using an ATLAS12 model atmosphere with He/H ratio 0.1 and the adopted solar parameters. The derived iron abundance, $\log \epsilon(\mathrm{Fe})$, versus the line's reduced equivalent width, $\log(W/\lambda)$, and its lower excitation potential (LEP), are shown in Figure [1](#), top and bottom panels, respectively. Inspection of Figure [1](#) (top panel) validates the adopted microturbulence as no trend is noticed in the derived Fe abundances with respect to $\log(W/\lambda)$. Similarly, inspection of Figure [1](#) (bottom panel) suggests no trend in the derived Fe abundances with respect to LEP, satisfying the excitation as well as the ionization balance for the adopted effective temperature and the surface gravity. Note that Fe I and Fe II lines with a range in their LEPs return similar Fe abundances by satisfying the excitation as well as the ionization balance. Hence, the above tests confirm and validate the adopted solar parameters, without any ambiguity, for conducting the abundance analysis.

In this study, we have primarily focused on the absorption features of neutral atomic lines of magnesium and carbon as well as molecular lines of their compounds involving hydrogen. Several Mg I atomic lines and MgH molecular lines of the MgH $A − X$ (0, 0) band, as well as C I atomic lines including a forbidden transition that is [C I] line at 8727.126 Å, CH molecular lines of the CH electronic ($A − X$) band, and C$_2$ molecular lines of the C$_2$ Swan (0, 0) band, were identified in the observed solar spectrum. These observed spectral features were accordingly subjected to equivalent width analyses and spectrum syntheses.

In this study, abundance analyses were conducted for the adopted solar parameters of model atmospheres having eight different He/H ratios: 0.075, 0.085, 0.100, 0.125, 0.135, 0.150, 0.175, and 0.200.

3.2.1. Molecular Lines

The spectrum synthesis code MOOG combined with ATLAS12 model atmospheres was used to synthesize MgH, CH, and C_2 Swan molecular lines present in the observed solar spectrum. For this purpose, the solar rotational velocity ($v \sin i$) and macroturbulent velocity (ξ_T) and the resolution of the observed solar spectrum at a given wavelength were required.

The adopted values for the solar rotational velocity ($v \sin i$) and macroturbulent velocity (ξ_T) are 1.7 km s^{-1} and 3.2 km s^{-1}, respectively. These values are in fair agreement with Pavlenko et al. (2012) for $v \sin i$ and with Hong et al. (2022) for ξ_T. The adopted resolution, derived from the resolving power of the observed solar spectrum, as represented by a Gaussian of FWHM is 0.02 Å at around 6500 Å.

Our adopted values for $v \sin i$ and ξ_T were obtained from the equivalent width analyses and the spectrum syntheses of the observed Fe I lines. The source of the required atomic data and the measured equivalent widths of these Fe I lines are discussed in Section 3.1. The measured equivalent width of an individual Fe I line provides the Fe abundance for the best adopted solar model with the parameters ($T_{\rm eff}$, $\log g$, [Fe/H], ξ_t) = (5773 K, 4.44 cgs, 0.0, 1.0 km s^{-1}). The absorption profile of the Fe I line is then synthesized for the above-derived Fe abundance combined with the adopted solar model. The best fit to the observed Fe I line is then obtained by tuning the two parameters, $v \sin i$ and ξ_T. This procedure is then followed for a set of observed Fe I lines to determine the mean $v \sin i$ and ξ_T. Synthesis of Fe I line at 6574.229 Å is shown in Figure 2(a) as an example.

MgH. The solar ^{24}MgH molecular lines for the $A - X$ (0, 0) molecular band are from Lambert et al. (1971). Lambert et al. (1971) note that all P branch ^{24}MgH lines are blended with ^{25}MgH and ^{26}MgH lines, and in their Table 1 the Q and R branch lines that are blended with ^{25}MgH or ^{26}MgH features are marked with asterisk. Note that P, Q, and R branches refer to different types of rovibronic molecular transitions and are classified based on the initial (J'') and final (J') state quantum numbers of the transition. The transition lines with $\Delta J = -1$ belong to the P branch. Similarly, $\Delta J = 0$ and $\Delta J = 1$ correspond to the Q and R branches, respectively (Banwell & McCash 1994).

For spectrum syntheses, we have selected a set of best MgH lines that are significant MgH contributors and are free or nearly free from other blends (see Table A1). The dissociation constant of MgH ($D_0 = 1.34$ eV) was sourced from the study of Hinkle et al. (2013). The solar isotopic ratio for magnesium, ^{24}Mg:^{25}Mg:^{26}Mg = 78.965:10.011:11.025, was adopted from Asplund et al. (2021). The LEP and $\log gf$ values for the selected lines are taken from the Kurucz database. Chris Sneden[3] has also reported fairly similar $\log gf$ and LEP values for ^{24}MgH lines, along with the wavelengths of corresponding ^{25}MgH and ^{26}MgH lines, generated from the data published by Hinkle et al. (2013).

To verify the adopted gf values, we have independently calculated the oscillator strengths (f values) using the relationship between f and the Einstein A coefficient (Equation (11.12), Gray 2021). The Einstein A coefficients were sourced from GharibNezhad et al. (2013), as in the Kurucz database, who calculated the A values by combining the experimental

---

[3] https://www.as.utexas.edu/~chris/mghpublic.txt

potential curves and energy levels with high-quality ab initio transition dipole moments using the relation defined by Bernath (2005). Note that our independently determined gf values are in excellent agreement with those adopted from the Kurucz database. This validation attests to the reliability of the Kurucz database for ^{24}MgH lines.

In the literature, we find that independent theoretical calculation by Kirby et al. (1979) and Weck et al. (2003) provides the band oscillator strength $f_{(0,0)}$ for the MgH $A - X$ (0, 0) molecular band. We note that, in the case of molecules, since the transitions are rovibronic (combined electronic, vibrational, and rotational transitions) in nature, these transitions possess two different oscillator strengths: band ($f_{(\nu',\nu'')}$) and rotational ($f_{(\nu'J',\nu''J'')}$) oscillator strengths. Oscillator strength defined for rovibronic transitions happening between two same or different vibrational levels is termed as band oscillator strength, whereas oscillator strength defined for rovibronic transitions happening between two different rotational levels belonging to two same or different vibrational levels is termed as rotational oscillator strength. In molecular transitions, the rotational oscillator strength is termed as the f value, and it, combined with the statistical weight of the initial energy level (g_i), gives the commonly used gf value (Masseron et al. 2014; Ram et al. 2014). $f_{(\nu',\nu'')}$ is related to $f_{(\nu'J',\nu''J'')}$ as follows (Weck et al. 2003):

$$f_{(\nu',\nu'')} = \frac{g_{J'J''}}{S_{J'}(J'')} \times f_{(\nu'J',\nu''J'')}, \qquad (3)$$

where $S_{J'}(J'')$ is defined as the Hönl–London factor. For the MgH $A - X$ (0, 0) band, the required $S_{J'}(J'')$ values for the P, Q, and R molecular branches, defined by Whiting & Nicholls (1974), are

$$S_{J'}(J'') = \begin{cases} \dfrac{(J'' - 1)}{2}, & J' = J'' - 1 \quad (\text{P-branch}) \\[2mm] \dfrac{(2J'' + 1)}{2}, & J' = J'' \qquad (\text{Q-branch}) \\[2mm] \dfrac{(J'' + 2)}{2}, & J' = J'' + 1 \quad (\text{R-branch}). \end{cases} \qquad (4)$$

Incorporating the $S_{J'}(J'')$ values from the abovementioned relation, band oscillator strength ($f_{(0,0)}$) of the MgH $A - X$ (0, 0) band was determined from our calculated rotational oscillator strengths, i.e., the f values. Hence, our independently determined f values above are actually the rotational oscillator strengths.

From Equation (3), we determine an average band oscillator strength $f_{(0,0)} = 0.1601$ that is found to be in excellent agreement with independent theoretical calculations by Kirby et al. (1979) and Weck et al. (2003) ($f_{(0,0)} = 0.161$). Henneker & Popkie (2003), using Hartree–Fock wave functions, derived a value of 0.250 for $f_{(0,0)}$. Using the multiconfiguration wave functions of Chan & Davidson (2003), Popkie (2003) calculated $f_{(0,0)} = 0.192$.

However, a significant lower value of $f_{(0,0)} = 0.055$ was determined by Lambert et al. (1971). To determine $f_{(0,0)}$, Lambert et al. (1971) fit a straight line to the observations in a standard plot of $\log (W_\lambda/S_{J'}(J''))$ versus $E_{J''}$ (W_λ: equivalent width and $E_{J''}$: LEP) for a number of ^{24}MgH lines present in the solar photosphere; the straight line fit to the plot is a model atmosphere prediction assuming LTE. Similarly, Grevesse & Sauval (1973) empirically determined $f_{(0,0)} = 0.035$ in order to
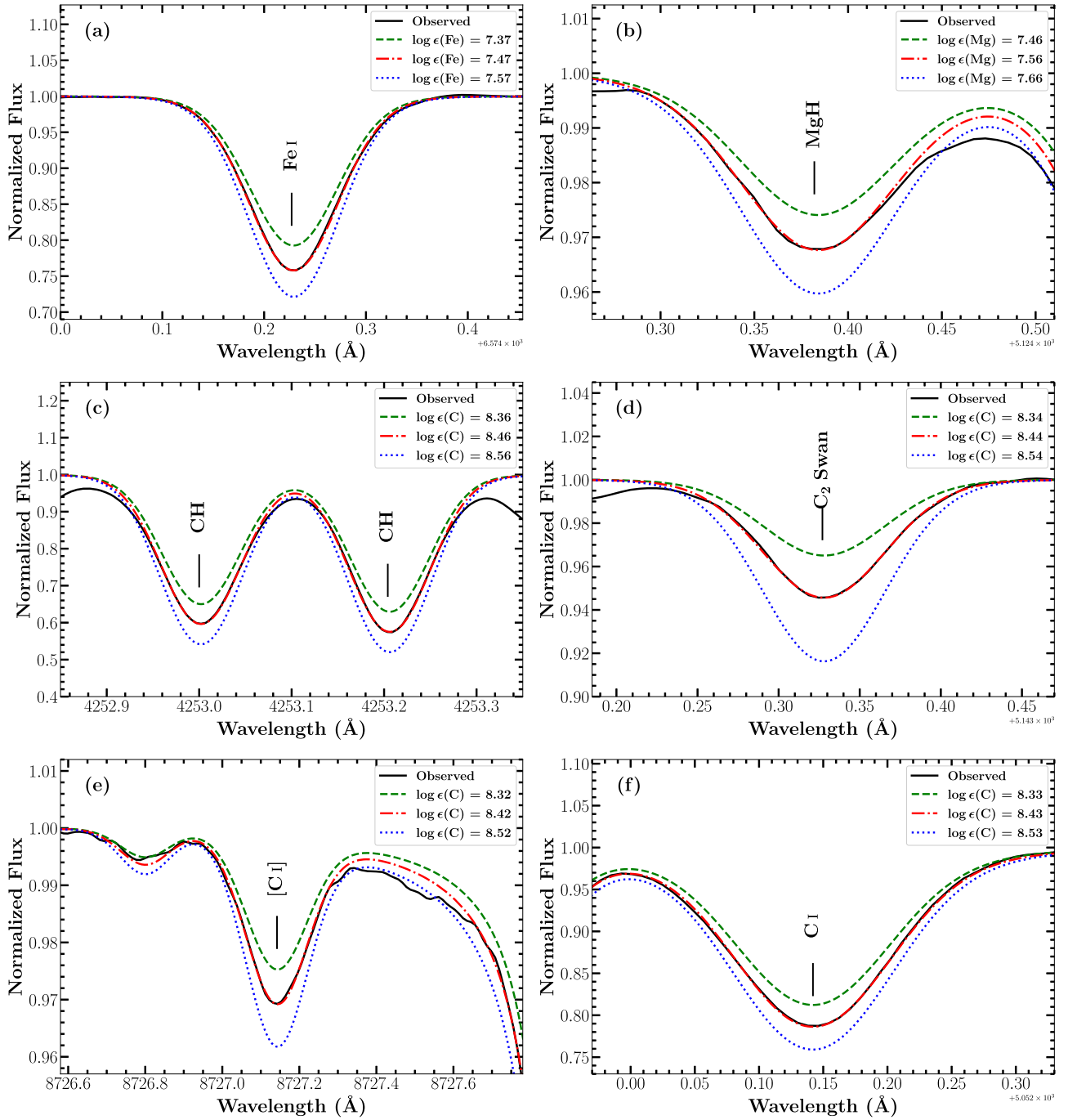
Figure 2. Syntheses of spectral lines of various species for He/H = 0.1. (a) Fe I line at 6574.229 Å. (b) MgH $A - X$ (0, 0) $R_1$13 line. (c) CH $A - X$ (0, 0) R_{2e}10 and R_{1f}10 lines. (d) C$_2$ Swan (0, 0) $R_1$11 line. (e) The forbidden [C I] line. (f) C I line at 5052.149 Å.

get the best agreement between the predicted and observed solar equivalent widths of ^{24}MgH lines. These discrepancies can be collectively attributed to the adopted solar magnesium abundance, the dissociation constant, and other uncertainties arising from the adopted solar model atmosphere.

After successfully verifying the rotational as well as the band oscillator strengths of the adopted solar ^{24}MgH molecular lines from the $A - X$ (0, 0) band, an abundance analysis for magnesium was performed using spectrum synthesis. A set of these MgH lines (see Table A1) was synthesized for eight different He/H ratios as mentioned above. Synthesis of MgH $A - X$ (0, 0) $R_1$13 line is shown in Figure 2(b) as an example.

CH. For spectrum synthesis, the solar CH molecular lines of the $A - X$ (0, 0) and (1, 1) molecular bands are adopted from Amarsi et al. (2021) (see Table A1). Three more CH $A - X$ (0, 0) lines at 4218.724, 4248.939, and 4356.361 Å, listed by Asplund et al. (2005b), were also added to our adopted line list from Amarsi et al. (2021). The LEP and the transition probability values for these individual lines are from Masseron et al. (2014). The dissociation constant for CH (D_0 = 3.465 eV) was sourced from Huber & Herzberg (1979). The solar isotopic ratio for carbon, ^{12}C:^{13}C = 98.893:1.107, was adopted from Asplund et al. (2021), and the wavelengths of corresponding ^{13}CH lines were taken from Masseron et al. (2014).

Table 1
Abundance of Mg and C Obtained from Their Key Species for Different He/H Models

He/H	Mg		C				
	$\log \epsilon(\text{Mg})_{\text{Mg I}}$	$\log \epsilon(\text{Mg})_{\text{MgH}}$	$\log \epsilon(\text{C})_{\text{C I}}$	$\log \epsilon(\text{C})_{[\text{C I}]}$	$\log \epsilon(\text{C})_{\text{C I} + [\text{C I}]}$	$\log \epsilon(\text{C})_{\text{CH }(A-X)}$	$\log \epsilon(\text{C})_{\text{C}_2 \text{ Swan}}$
0.075	7.60 ± 0.06	7.52 ± 0.05	8.48 ± 0.03	8.44	8.47 ± 0.03	8.43 ± 0.02	8.43 ± 0.02
0.085	7.57 ± 0.06	7.53 ± 0.05	8.45 ± 0.04	8.43	8.45 ± 0.04	8.44 ± 0.02	8.43 ± 0.02
0.100	7.55 ± 0.06	7.54 ± 0.05	8.42 ± 0.04	8.42	8.42 ± 0.04	8.44 ± 0.02	8.43 ± 0.02
0.125	7.53 ± 0.06	7.56 ± 0.05	8.38 ± 0.04	8.41	8.38 ± 0.04	8.46 ± 0.02	8.43 ± 0.02
0.135	7.51 ± 0.05	7.58 ± 0.05	8.34 ± 0.05	8.40	8.35 ± 0.05	8.47 ± 0.02	8.43 ± 0.02
0.150	7.50 ± 0.05	7.59 ± 0.05	8.30 ± 0.05	8.40	8.32 ± 0.06	8.48 ± 0.02	8.43 ± 0.02
0.175	7.47 ± 0.05	7.62 ± 0.05	8.25 ± 0.05	8.39	8.27 ± 0.07	8.50 ± 0.02	8.43 ± 0.02
0.200	7.45 ± 0.05	7.64 ± 0.05	8.21 ± 0.05	8.37	8.23 ± 0.08	8.52 ± 0.02	8.43 ± 0.02

Amarsi et al. (2021) used the LEP and $\log gf$ values sourced from Masseron et al. (2014), while Asplund et al. (2005b) adopted these values from Folomeg et al. (1987). We found that the values listed in both sources are in good agreement with each other. Hence, we adopted the values provided by Masseron et al. (2014) as it is the most recent source. Syntheses of CH $A - X$ (0, 0) $R_{2e}10$ and $R_{1f}10$ lines are shown in Figure 2(c) as examples.

C_2 Swan. The solar C_2 Swan molecular lines of the (0, 0) molecular band are from Asplund et al. (2005b) (see Table A5). The dissociation constant value ($D_0 = 6.297$ eV) is from Urdahl et al. (1991). The solar carbon isotopic ratio, adopted for CH molecular lines, was also applied to the C_2 Swan molecular lines. The wavelengths of corresponding $^{12}C^{13}C$ lines were taken from Brooke et al. (2013). For the analysis, we have considered three different sources that provide the $\log gf$ values for the C_2 Swan (0, 0) transitions. These are Grevesse et al. (1991), Hema et al. (2012), and Brooke et al. (2013). Grevesse et al. (1991) provide values from measurements of the $d^3\Pi_g$ molecular state's radiative lifetime. Hema et al. (2012) provide gf values that are from the theoretical band oscillator strengths computed by Schmidt & Bacskay (2007). Brooke et al. (2013)'s study is the latest in the literature and is based on ab initio calculation of the transition dipole moment function. These three sources also provide the transition's LEP but note that its gf value as well as the LEP differs from one source to another.

An abundance analysis of carbon was conducted by synthesizing the C_2 Swan transitions using the standard ATLAS12 solar model atmosphere for He/H ratio 0.1. These three sources provide three different pairs of (LEP, $\log gf$). The best fit to the observed C_2 Swan transition hence provides the carbon abundance. Note that the carbon abundances derived from these three different sources are in good agreement within 0.05 dex. In this study, we finally adopt Brooke et al. (2013)'s values for the subsequent abundance analysis of carbon. Synthesis of C_2 Swan (0, 0) $R_1 11$ line is shown in Figure 2(d) as an example.

3.2.2. Atomic Lines

Mg I. An equivalent width analysis was conducted for the measured equivalent widths of neutral magnesium (Mg I) lines (see Table A2). The atomic data for these transitions, for example, the line's wavelength, the LEP, and the transition probability, i.e., the $\log gf$ value, are from two sources: Scott et al. (2015) and Asplund et al. (2021). Both Scott et al. (2015) and Asplund et al. (2021) provide the measured equivalent widths of these observed transitions in the Sun, and for the

common lines, these are in excellent agreement with our measurements using the FTS solar spectrum. Asplund et al. (2021)'s list includes two additional lines of Mg I at 8712.689 and 8717.825 Å and adopts the recent $\log gf$ values from Pehlivan Rhodin et al. (2017).

Our analyses of both these lists confirm that the derived Mg abundances are in excellent agreement; however, the line-to-line scatter is larger for Scott et al. (2015)'s list. Hence, we adopted Asplund et al. (2021)'s list, and Mg abundances were derived for eight different He/H ratios as mentioned above. In this study, one more Mg I line at 5711.088 Å was added to Asplund et al. (2021)'s list as this line was found to be clean and without blends; the $\log gf$ value is from Pehlivan Rhodin et al. (2017), and the LEP is from the NIST Atomic Spectra Database.[4]

C I and [C I]. An abundance analysis was conducted for the neutral carbon lines; both permitted (C I) and forbidden [C I] lines were considered (see Table A3). The measured equivalent widths including the atomic data are from Amarsi et al. (2019). Note that the infrared lines were excluded from our LTE analysis as these lines exhibit severe departures from LTE (Asplund et al. 2005b).

The adopted equivalent widths are in excellent agreement with our measurements, except for the forbidden carbon [C I] line. Our measured equivalent width for the [C I] line is, however, close to Lambert (1978)'s measured value of 6.5 mÅ. Hence, we adopt Lambert (1978)'s measurement over Amarsi et al. (2019), that is, 4.7 mÅ, for the [C I] line.

Finally, carbon abundances were derived from all these line transitions for eight different He/H ratios. We have derived the abundances using the equivalent width analysis as well as the spectrum synthesis. The derived abundances from both of these methods are in excellent agreement. Nevertheless, we report the derived abundances obtained from spectrum synthesis. Syntheses of the forbidden [C I] line and the permitted C I line at 5052.149 Å are shown in Figures 2(e) and (f), respectively, as examples.

3.3. Determination of the Solar He/H Ratio

Table 1 illustrates the abundance of magnesium obtained from Mg I atomic lines as well as from MgH molecular lines. Eight sets of Mg abundances are listed for the adopted eight different He/H ratios (see Table 1). Similarly, Table 1 also illustrates eight sets of carbon abundances derived from neutral carbon transitions, both permitted and forbidden, and from molecular lines of CH and C_2 Swan.

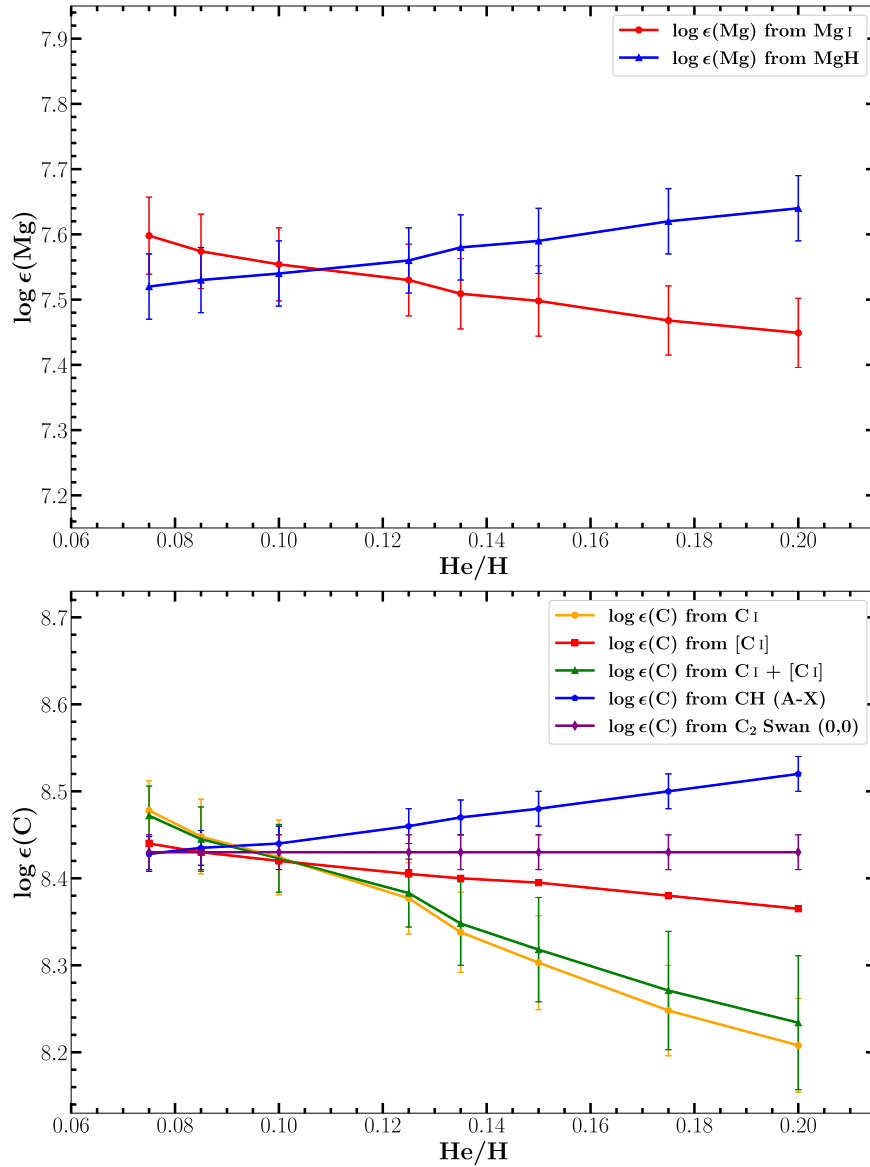[4] https://www.nist.gov/pml/atomic-spectra-database

Figure 3. Abundance of magnesium obtained from Mg I and MgH lines for different He/H ratios (top panel). Abundance of carbon obtained from C I, CH, and C_2 Swan lines for different He/H ratios (bottom panel).

Mg and C abundances, derived from their observed atomic and molecular absorptions, versus the adopted model's He/H ratios are shown in Figure 3, top and bottom panels, respectively. An examination of the Figure 3, top and bottom panels, suggests that the derived Mg and C abundances depend on the adopted model's He/H ratio except for the derived C abundance from C_2 Swan transitions. It is worth noting that for a higher He/H ratio, the derived Mg and C abundances from their observed atomic lines are lower than those derived for a lower He/H ratio. However, the derived Mg and C abundances from their respective hydrides exhibit an inverse trend—see Figure 3, top and bottom panels. These trends are as expected due to the adopted model's He/H ratio; decreasing the abundance of hydrogen or increasing the abundance of helium, i.e., increasing the He/H ratio, results in a decrease in continuous opacity per gram (Sumangala Rao et al. 2011) along with a decrease in the availability of hydrogen atoms to form metal hydrides. Therefore, for the same observed strength of the atomic line, the elemental abundance must decrease

(Hema et al. 2020). But for a metal hydride line, a combined effect of the reduced continuum absorption and the line's reduced absorption strength demands an increased metal abundance to fit the same observed line strength.

In principle, the abundances of magnesium and carbon obtained from their respective atomic and molecular lines must return the same abundances within the measured uncertainty. Here, we note that the rms errors in abundances due to line-to-line scatter dominate over the other measurement errors. For example, the uncertainty in measuring the equivalent width or the errors associated with the parameters involving the spectrum syntheses are not very significant. We infer the He/H ratios of $0.108^{+0.051}_{-0.046}$ and $0.091^{+0.019}_{-0.014}$ as the best-determined values from Mg and C abundance analyses, respectively—see Figure 3, top and bottom panels. The uncertainties in the derived He/H ratios are translated from the rms uncertainties in abundances associated with the atomic and molecular hydride features of Mg and C. For the adopted range in the He/H values—see Figure 3, top and bottom panels—note the divergence in the

Table 2
Comparison of Abundances Derived Using 1D LTE Model Atmosphere for
He/H = 0.1: ATLAS12 (This Work) and Asplund et al. (2021)

Abundance	Species	This Work ATLAS12	Asplund et al. (2021)	
			MARCS	HM
$\log \epsilon$ (Fe)	Fe I	7.43 ± 0.05	7.41 ± 0.04	7.48 ± 0.05
	Fe II	7.43 ± 0.07	7.38 ± 0.04	7.43 ± 0.03
$\log \epsilon$ (Mg)	Mg I	7.55 ± 0.06	7.52 ± 0.02	7.57 ± 0.03
	MgH	7.54 ± 0.05	...	...
$\log \epsilon$ (C)	[C I]	8.42	8.42	8.43
	C I	8.42 ± 0.04	8.46 ± 0.04	8.50 ± 0.04
	CH (A − X)	8.44 ± 0.02	8.40 ± 0.05	8.56 ± 0.05
	C₂ Swan	8.43 ± 0.02	8.43 ± 0.03	8.52 ± 0.03

derived Mg and C abundances from their respective features and the associated abundance uncertainties. For this study, we adopted models with a range in their He/H values: 0.075 $\leqslant$ He/H $\leqslant$ 0.200; more weight is given to the abundance analyses of C than to that of Mg due to the lower uncertainties in the derived C abundances.

4. Conclusion and Discussions

In Table 2, we compare the derived abundances of the key species using three different solar one-dimensional LTE model atmospheres: ATLAS12 (this study), MARCS,[5] and Holweger–Müller (HM).[6] The derived abundances in Table 2 are for the solar model with He/H = 0.1. Table 2 clearly demonstrates that the derived abundances in this study are in excellent agreement with that of Asplund et al. (2021).

Lodders (2003) suggested present-day solar helium abundance of $\log \epsilon$ (He) = 10.899 ± 0.005 from averaging helium abundance values obtained from various helioseismic studies over the years. Basu & Antia (2004) have also derived the solar helium mass fraction, $Y_\odot$, as 0.2485 ± 0.0034 using helioseismology, which corresponds to a He/H ratio of 0.085 or $\log \epsilon$ (He) = 10.93 ± 0.01. With the improved SAHA-S3 equation of state, Vorontsov et al. (2014) derived a range for the solar helium mass fraction, $Y_\odot$, as 0.240–0.255.

Asplund et al. (2021) has reported $Y_\odot$ = 0.2423 ± 0.0054 by taking the mean of Basu & Antia (2004) and Vorontsov et al. (2014). This corresponds to a He/H ratio of 0.082 or $\log \epsilon$ (He) = 10.914 ± 0.013.

Our results determined from the observed absorptions of Mg I and MgH and that of C I and CH are consistent: He/H = $0.108^{+0.051}_{-0.046}$ and $0.091^{+0.019}_{-0.014}$ from the abundance analyses of Mg and C, respectively. Our derived He/H ratios are in fair agreement with the result obtained through various helioseismological studies, signifying the reliability and accuracy of our novel technique in determining the solar helium-to-hydrogen ratio. This study also confirms that the widely assumed and adopted (He/H)$_\odot$ = 0.1 is in fair agreement with our measurements. More reliable values should, in principle, come from 3D model atmospheres with full non-LTE calculations.

---

[5] The theoretical hydrostatic model computed using the MARCS code (Gustafsson et al. 2008).
[6] The semi-empirical Holweger–Müller model (Holweger & Mueller 1974), upgraded from the Holweger (1967) version using updated equation of state and continuous opacities (Asplund et al. 2009).

Using our derived He/H ratio ($0.091^{+0.019}_{-0.014}$) and Asplund et al. (2021)'s $(Z/X)_\odot$ value, we have determined the solar mass fraction as $X_\odot = 0.7232^{+0.0305}_{-0.0377}$, $Y_\odot = 0.2633^{+0.0384}_{-0.0311}$, and $Z_\odot = 0.0135^{+0.0006}_{-0.0007}$. These values strongly constrain the modeling of the structure and evolution of the Sun. It will be interesting to see whether the standard stellar evolution model constructed with our deduced values of $X_\odot$, $Y_\odot$, and $Z_\odot$ can reproduce the present solar luminosity $L_\odot$ at the present solar age $t_\odot$.

Acknowledgments

Appendix
Line Lists of Mg I, MgH, C I, CH, and C₂ Swan Spectral Lines

The following tables provide the complete line lists of MgH (Table A1), CH (Table A2), C₂ Swan (Table A3), Mg I (Table A4), and C I (Table A5) adopted in this study, along with the derived abundances for He/H = 0.1.

Table A1
Abundance of Mg Derived from MgH $A − X$ (0, 0) Molecular Lines for
He/H = 0.1

λ (Å)	Branch	LEP (eV)	$\log gf$	$\log \epsilon$ (Mg)
5124.411	$R_1 13$	0.128	0.105	7.56
5153.680	$Q_1 18$	0.238	0.486	7.50
5198.326	$P_2 26$	0.478	0.274	7.55
5201.636	$P_1 6$	0.030	−0.346	7.48
5202.985	$P_1 24$	0.411	0.261	7.47
5207.083	$P_2 21$	0.319	0.183	7.60
5209.590	$P_1 19$	0.264	0.165	7.58

avg. $\log \epsilon$ (Mg) = 7.54 ± 0.05

Table A2
Abundance of C Derived from CH Molecular Lines for He/H = 0.1

λ (Å)	Band	Branch	LEP (eV)	$\log gf$	$\log \epsilon$ (C)
4218.723	$A − X(0, 0)$	$R_{2e} 15$	0.411	−1.008	8.41
4248.945	$A − X(0, 0)$	$R_{1f} 15$	0.189	−1.431	8.47
4253.003	$A − X(1, 1)$	$R_{2e} 10$	0.523	−1.506	8.46
4253.209	$A − X(1, 1)$	$R_{1f} 10$	0.523	−1.471	8.46
4255.252	$A − X(0, 0)$	$R_{1f} 9$	0.157	−1.455	8.43
4263.976	$A − X(1, 1)$	$R_{2e} 8$	0.460	−1.575	8.43
4274.186	$A − X(0, 0)$	$R_{1e} 6$	0.074	−1.563	8.46
4356.375	$A − X(0, 0)$	$P_{2f} 9$	0.155	−1.846	8.43
4356.600	$A − X(0, 0)$	$P_{1e} 9$	0.157	−1.793	8.44

avg. $\log \epsilon$ (C) = 8.44 ± 0.02

Table A3
Abundance of C Derived from C_2 Swan (0, 0) Molecular Lines for He/H = 0.1

λ (Å)	Branch	LEP (eV)	log gf	log ϵ(C)
5033.700	$R_3$50	0.508	0.193	8.44
5073.600	$R_3$39	0.312	0.082	8.45
5109.300	$R_3$27	0.152	−0.082	8.41
5132.500	$R_2$17	0.062	−0.262	8.43
5136.600	$R_3$15	0.049	−0.341	8.38
5140.400	$R_3$13	0.037	−0.404	8.45
5143.300	$R_1$11	0.026	−0.409	8.44
5144.900	$R_1$10	0.022	−0.445	8.43
			avg. log ϵ(C) = 8.43 ± 0.02	

Table A4
Abundance of Mg Derived from Mg I Atomic Lines for He/H = 0.1
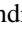
λ (Å)	LEP (eV)	log gf	EW (mÅ)	log ϵ(Mg)
5711.088	4.346	−1.742	113.5	7.51
6318.716	5.108	−2.020	41.3	7.54
6319.236	5.108	−2.242	26.0	7.50
8712.689	5.932	−1.152	68.0	7.57
8717.825	5.933	−0.930	100.0	7.59
8923.569	5.394	−1.679	63.3	7.64
9429.814	5.932	−1.306	47.1	7.48
9983.200	5.932	−2.177	10.0	7.55
10312.531	6.118	−1.718	18.3	7.51
11522.240	6.118	−1.913	21.0	7.67
12417.937	5.932	−1.662	44.8	7.55
12423.029	5.932	−1.185	97.0	7.55
			avg. log ϵ(Mg) = 7.55 ± 0.06	

Table A5
Abundance of C Derived from C I Atomic Lines for He/H = 0.1

λ (Å)	LEP (eV)	log gf	log ϵ(C)
8727.126[a]	1.264	−8.165	8.42
5052.149	7.685	−1.303	8.43
5380.331	7.685	−1.616	8.48
6587.608	8.537	−1.003	8.38
7111.475	8.640	−1.085	8.37
7113.180	8.647	−0.773	8.46
		avg. log ϵ(C) = 8.42 ± 0.04	

Note.
[a] Forbidden line.

ORCID iDs

Satyajeet Moharana ⬤ https://orcid.org/0009-0007-9411-0284
B. P. Hema ⬤ https://orcid.org/0000-0002-0160-934X
Gajendra Pandey ⬤ https://orcid.org/0000-0001-5812-1516

References

Allende Prieto, C. 2020, JApA, 41, 41
Allende Prieto, C., & Garcia Lopez, R. J. 1998, A&AS, 131, 431
Amarsi, A. M., Barklem, P. S., Collet, R., Grevesse, N., & Asplund, M. 2019, A&A, 624, A111
Amarsi, A. M., Grevesse, N., Asplund, M., & Collet, R. 2021, A&A, 656, A113
Anders, E., & Grevesse, N. 1989, GeCoA, 53, 197
Asplund, M., Amarsi, A. M., & Grevesse, N. 2021, A&A, 653, A141
Asplund, M., Grevesse, N., & Sauval, A. J. 2005a, in ASP Conf. Ser. 336, Cosmic Abundances as Records of Stellar Evolution and Nucleosynthesis, ed. T. G. Barnes, III & F. N. Bash (San Francisco, CA: ASP), 25
Asplund, M., Grevesse, N., Sauval, A. J., Allende Prieto, C., & Blomme, R. 2005b, A&A, 431, 693
Asplund, M., Grevesse, N., Sauval, A. J., & Scott, P. 2009, ARA&A, 47, 481
Asplund, M., Nordlund, Å., Trampedach, R., & Stein, R. F. 2000, A&A, 359, 743
Banwell, C., & McCash, E. 1994, Fundamentals of Molecular Spectroscopy (New York: McGraw-Hill)
Basu, S., & Antia, H. M. 2004, ApJL, 606, L85
Basu, S., & Antia, H. M. 2008, PhR, 457, 217
Bernath, P. F. 2005, Spectra of Atoms and Molecules (2nd ed.; New York: Oxford Univ. Press)
Brooke, J. S. A., Bernath, P. F., Schmidt, T. W., & Bacskay, G. B. 2013, JQSRT, 124, 11
Caffau, E., Ludwig, H. G., Steffen, M., Freytag, B., & Bonifacio, P. 2011, SoPh, 268, 255
Chan, A. C. H., & Davidson, E. R. 2003, JChPh, 52, 4108
Folomeg, B., Rosmus, P., & Werner, H.-J. 1987, CPL, 136, 562
GharibNezhad, E., Shayesteh, A., & Bernath, P. F. 2013, MNRAS, 432, 2043
Goldberg, L., Muller, E. A., & Aller, L. H. 1960, ApJS, 5, 1
Gray, D. F. 2021, The Observation and Analysis of Stellar Photospheres (4th ed.; Cambridge: Cambridge Univ. Press)
Grevesse, N., Lambert, D. L., Sauval, A. J., et al. 1991, A&A, 242, 488
Grevesse, N., & Sauval, A. J. 1973, A&A, 27, 29
Grevesse, N., & Sauval, A. J. 1998, SSRv, 85, 161
Gustafsson, B., Edvardsson, B., Eriksson, K., et al. 2008, A&A, 486, 951
Hema, B. P., & Pandey, G. 2014, ApJL, 792, L28
Hema, B. P., Pandey, G., Kurucz, R. L., & Allende Prieto, C. 2020, ApJ, 897, 32
Hema, B. P., Pandey, G., & Lambert, D. L. 2012, ApJ, 747, 102
Hema, B. P., Pandey, G., & Srianand, R. 2018, ApJ, 864, 121
Henneker, W. H., & Popkie, H. E. 2003, JChPh, 54, 1763
Hinkle, K., Wallace, L., Valenti, J., & Harmer, D. 2000, Visible and Near Infrared Atlas of the Arcturus Spectrum 3727-9300 A (San Francisco, CA: ASP)
Hinkle, K. H., Wallace, L., Ram, R. S., et al. 2013, ApJS, 207, 26
Hirshberg, J. 1973, RvGSP, 11, 115
Holweger, H. 1967, ZA, 65, 365
Holweger, H., & Mueller, E. A. 1974, SoPh, 39, 19
Hong, J., Qiu, Y., Hao, Q., et al. 2022, A&A, 668, A9
Houdek, G., & Gough, D. O. 2007, MNRAS, 375, 861
Huber, K. P., & Herzberg, G. 1979, Constants of Diatomic Molecules (Berlin: Springer), 8
Kirby, K., Saxon, R. P., & Liu, B. 1979, ApJ, 231, 637
Kurucz, R. L. 2014, Determination of Atmospheric Parameters of B-, A-, F- and G-Type Stars (Berlin: Springer), 39
Kurucz, R. L., Furenlid, I., Brault, J., & Testerman, L. 1984, Solar Flux Atlas from 296 to 1300 nm (Sunspot, NM: National Solar Observatory)
Lambert, D. L. 1967, Natur, 215, 43
Lambert, D. L. 1968, MNRAS, 138, 143
Lambert, D. L. 1978, MNRAS, 182, 249
Lambert, D. L., Mallia, E. A., & Petford, A. D. 1971, MNRAS, 154, 265
Laming, J. M. 2015, LRSP, 12, 2
Lodders, K. 2003, ApJ, 591, 1220
Masseron, T., Plez, B., Van Eck, S., et al. 2014, A&A, 571, A47
Monteiro, M. J. P. F. G., & Thompson, M. J. 2005, MNRAS, 361, 1187
Nieva, M. F., & Przybilla, N. 2012, A&A, 539, A143
Ogilvie, K. W., & Wilkerson, T. D. 1969, SoPh, 8, 435
Pavlenko, Y. V., Jenkins, J. S., Jones, H. R. A., Ivanyuk, O., & Pinfield, D. J. 2012, MNRAS, 422, 542
Pehlivan Rhodin, A., Hartman, H., Nilsson, H., & Jönsson, P. 2017, A&A, 598, A102
Popkie, H. E. 2003, JChPh, 54, 4597
Ram, R. S., Brooke, J. S. A., Bernath, P. F., Sneden, C., & Lucatello, S. 2014, ApJS, 211, 5
Reames, D. V. 2021, Solar Energetic Particles: A Modern Primer on Understanding Sources, Acceleration and Propagation, Vol. 978 (Berlin: Springer)
Russell, H. N. 1929, ApJ, 70, 11
Schmidt, T. W., & Bacskay, G. B. 2007, JChPh, 127, 234310
Scott, P., Grevesse, N., Asplund, M., et al. 2015, A&A, 573, A25

Sneden, C., Bean, J., Ivans, I., Lucatello, S., & Sobeck, J. 2012, MOOG: LTE Line Analysis and Spectrum Synthesis, Astrophysics Source Code Library, ascl:1202.009

Suess, H. E., & Urey, H. C. 1956, RvMP, 28, 53

Sumangala Rao, S., Pandey, G., Lambert, D. L., & Giridhar, S. 2011, ApJL, 737, L7

Urdahl, R. S., Bao, Y., & Jackson, W. M. 1991, CPL, 178, 425

Vorontsov, S. V., Baturin, V. A., Ayukov, S. V., & Gryaznov, V. K. 2014, MNRAS, 441, 3296

Weck, P. F., Schweitzer, A., Stancil, P. C., Hauschildt, P. H., & Kirby, K. 2003, ApJ, 582, 1059

Whiting, E. E., & Nicholls, R. W. 1974, ApJS, 27, 1